

Model. We start by introducing a lattice model that reproduces the dynamics of a Yang-Mills gauge theory with dynamical fermionic matter in the continuum limit [14, 26, 42, 43]. In this work, the Yang-Mills theory is formulated on a d -dimensional discrete spatial lattice with lattice spacing a . We denote lattice sites in d dimensions by their coordinate vector $x \in \mathbb{R}^d$ and edges (also called links) between sites by the tuple (x, k) where x is a lattice site and $k \in \{1, \dots, d\}$ is a direction. The (single flavor) fermionic particles reside on the lattice sites x , while the gauge fields live on the links. The Yang-Mills Hamiltonian $\hat{H}_{\text{YM}} = \hat{H}_{\text{hopp}} + \hat{H}_{\text{mass}} + \hat{H}_{\text{plaq}} + \hat{H}_{\text{elec}} + \hat{H}_{\text{wilson}}$ in the temporal gauge reads

$$\begin{aligned} \hat{H}_{\text{YM}} = & \sum_{\text{sites}} \sum_k \frac{1}{2a} \left(\hat{\psi}_x [i\gamma^k + r] \hat{U}_{(x,k)} \hat{\psi}_{x+k} + \text{h.c.} \right) \\ & + \sum_{\text{sites}} \left(m + \frac{rd}{a} \right) \hat{\psi}_x \hat{\psi}_x - \frac{a^{d-4}}{2g^2} \sum_{\text{plaq.}} \text{Tr} \left(\hat{U}_{\square} + \hat{U}_{\square}^{\dagger} \right) \\ & + \frac{g^2 a^{2-d}}{4} \sum_{\text{links}} \sum_{\alpha} \left((\hat{L}_{(x,k)}^{\alpha})^2 + (\hat{R}_{(x,k)}^{\alpha})^2 + \theta_k^{\alpha} \right), \quad (1) \end{aligned}$$

where γ^k are given by the Dirac gamma matrices and where m, g denote the fermionic mass parameter and the gauge field coupling parameter, respectively. This Hamiltonian mainly consists of four contributing terms describing the fermionic matter and gauge field energies and their interactions [44]. An additional term \hat{H}_{wilson} is introduced via the parameter r which acts as a regulator to avoid the fermion doubling problem [45, 46]. The quantities $\hat{\psi}_x$ and $\hat{\bar{\psi}}_x = \hat{\psi}_x^{\dagger} \gamma^0$ represent the fermionic field operators that carry implicit spinor- and color component indices $i, j \in \{1, \dots, 2^{\lceil d/2 \rceil}\}$ and $b, c \in \{1, \dots, \dim(R)\}$ respectively, where $\dim(R)$ denotes the dimension of the representation R of the corresponding gauge group G . For example, in the case of $G = SU(N)$ in the fundamental representation, we have $\dim(R) = N$. Note that we whenever the spinor- and color indices are suppressed, we implicitly sum over all these indices. The fermionic operators satisfy the standard anti-commutation relations $\{\hat{\psi}_x^{b,i}, \hat{\psi}_y^{\dagger c,j}\} = \delta_{xy} \delta_{bc} \delta_{ij}$, $\{\hat{\psi}_x^{b,i}, \hat{\psi}_y^{c,j}\} = 0$. The gauge field operators $\hat{U}_{(x,k)}$ on a link (x, k) have the same structure as the generators T^{α} of the gauge group: They are $\dim(R) \times \dim(R)$ dimensional matrices whose entries $(\hat{U}_{(x,k)})_{mn}$ are operators that act on the link Hilbert space. The plaquette operators are defined by $\hat{U}_{\square} = \hat{U}_{(x,k)} \hat{U}_{(x+k,l)} \hat{U}_{(x+l,k)}^{\dagger} \hat{U}_{(x,l)}^{\dagger}$, and the trace of these operators appearing in \hat{H}_{YM} is only taken in the Lie algebra space of the group generators T^{α} and does not extend to the quantum Hilbert space. The conjugate link flux variables $\hat{L}_{(x,k)}^{\alpha}$ and $\hat{R}_{(x,k)}^{\alpha}$ are associated with the left end and the right end of a link (x, k) , respectively, and are defined through the commutation relations $[\hat{L}_{(x,k)}^{\alpha}, \hat{U}_{(x,k)}] = T^{\alpha} \hat{U}_{(x,k)}$, $[\hat{R}_{(x,k)}^{\alpha}, \hat{U}_{(x,k)}] = \hat{U}_{(x,k)} T^{\alpha}$ [47]. Note that in the case of QED, these two

variables reduce to the electric flux field operators $\hat{E}_{(x,k)}$ used in [26]. In addition, a constant background gauge field is introduced via the constant parameters θ_k^{α} [48]. Note that all operators assigned to different lattice sites or links commute with each other. The Gauss law operators are defined by

$$\hat{G}_x^{\alpha} = \sum_k \left(\hat{L}_{(x,k)}^{\alpha} - \hat{R}_{(x-k,k)}^{\alpha} \right) - \hat{\psi}_x^{\dagger} T^{\alpha} \hat{\psi}_x \quad (2)$$

and they specify the gauge-invariant states $|\phi_{\text{phys}}\rangle$ that span the physical sector $\mathcal{H}^{\text{phys}}$ of the total Hilbert space via $\hat{G}_x^{\alpha} |\phi_{\text{phys}}\rangle = 0$ for all lattice sites x and $\alpha \in \{1, \dots, \dim(G)\}$. The Gauss law operators are the generators of local (time-independent) gauge transformations and commute with the Hamiltonian $[\hat{H}_{\text{YM}}, \hat{G}_x^{\alpha}] = 0$, implying that the gauge-invariance is in principle conserved in a real-time evolution. Finally, the Hilbert space \mathcal{H}_{YM} on which the Hamilton operator \hat{H}_{YM} acts is given by $\mathcal{H}_{\text{YM}} = \bigotimes_{x,k} \mathcal{H}_x^{\text{fermi}} \otimes \mathcal{H}_{(x,k)}^{\text{gauge}}$, where the individual (fermionic) Hilbert spaces at each lattice site x have dimension $\dim(\mathcal{H}_x^{\text{fermi}}) = 2^{2^{\lceil d/2 \rceil}} \dim(R)$, while the dimension of the (bosonic) link Hilbert spaces $\mathcal{H}_{(x,k)}^{\text{gauge}}$ generally depends on a chosen truncation of the gauge fields [20, 47, 49]. The physical states $|\phi_{\text{phys}}\rangle$ which preserve the Gauss law constraints span the physical Hilbert subspace $\mathcal{H}^{\text{phys}} \subset \mathcal{H}_{\text{YM}}$.

Gauge-invariant state preparation. Heuristic state preparation ansätze [25], which are common for example in quantum chemistry applications [50, 51], fail to sample efficiently from $\mathcal{H}^{\text{phys}}$ (see Supplementary Material [44]).

To circumvent this problem, we construct parametrized trial states tailored to the gauge symmetry of the theory. To do so, we look for unitary operators $\hat{\mathcal{O}}$ that map the physical Hilbert space $\mathcal{H}^{\text{phys}}$ onto itself, i.e. $\hat{\mathcal{O}} |\phi_{\text{phys}}\rangle \in \mathcal{H}^{\text{phys}}$ for all $|\phi_{\text{phys}}\rangle \in \mathcal{H}^{\text{phys}}$. We call unitary operators with this property *gauge invariant*. A parametrized family $\hat{\mathcal{U}}(\boldsymbol{\theta})$, with real parameter vector $\boldsymbol{\theta}$, of gauge invariant operators then allows us to construct trial states from any initial state $|\phi_{\text{init}}\rangle \in \mathcal{H}^{\text{phys}}$ via $|\phi(\boldsymbol{\theta})\rangle = \hat{\mathcal{U}}(\boldsymbol{\theta}) |\phi_{\text{init}}\rangle$. The definition of $\mathcal{H}^{\text{phys}}$ implies that a family of unitary operators $\hat{\mathcal{U}}(\boldsymbol{\theta})$ is gauge invariant if and only if it commutes with the Gauss law operators \hat{G}_x^{α} in Eq. (2), $[\hat{\mathcal{U}}(\boldsymbol{\theta}), \hat{G}_x^{\alpha}] = 0$ for all $\boldsymbol{\theta}, \alpha, x$. With this choice, it follows that a parametrized trial state $|\phi(\boldsymbol{\theta})\rangle$ is gauge invariant if and only if the initial state $|\phi_{\text{init}}\rangle$ is chosen to be gauge invariant since $\hat{G}_x^{\alpha} |\phi(\boldsymbol{\theta})\rangle = \hat{\mathcal{U}}(\boldsymbol{\theta}) \hat{G}_x^{\alpha} |\phi_{\text{init}}\rangle = 0$. As a result, such a gauge-invariant variational form will sample from the physical Hilbert space only. Furthermore, note that if an Hermitian operator commutes with the Gauss law operators $[\hat{F}, \hat{G}_x^{\alpha}] = 0$, then the exponential of \hat{F} is a unitary operator that commutes with the Gauss law operators, $[\exp(i\hat{F}), \hat{G}_x^{\alpha}] = 0$, too [52].

Following these prescriptions, a parametrized family of gauge-invariant unitary operators $\hat{\mathcal{U}}(\boldsymbol{\theta})$ can be gener-

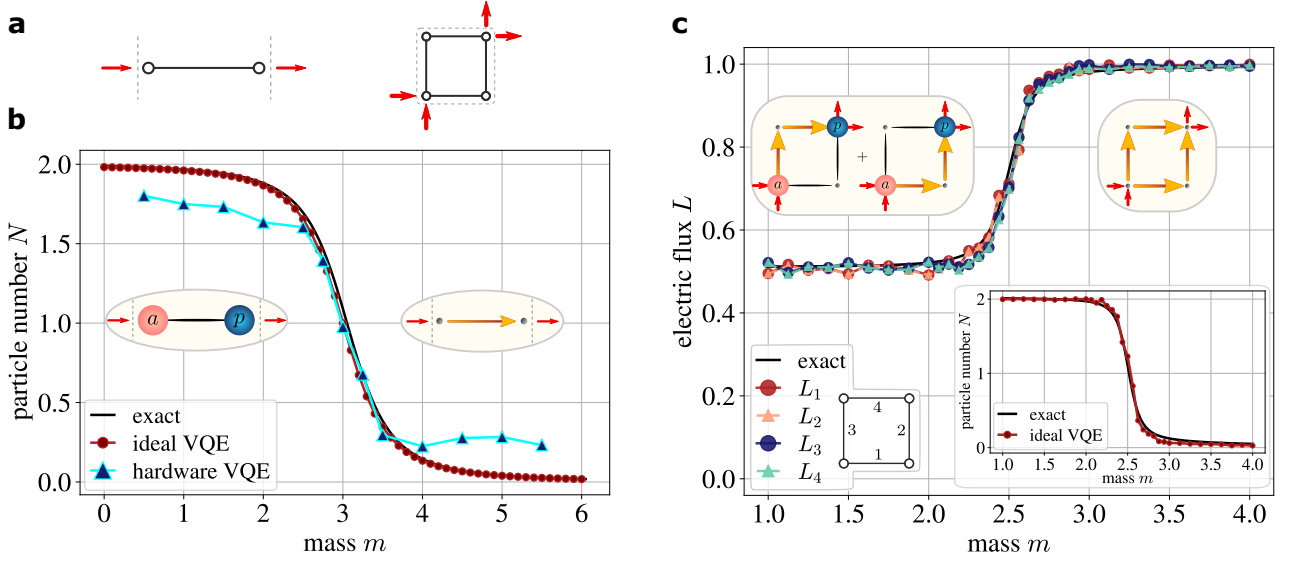


FIG. 1. Ground state search in a (1+1)- and (2+1)-dimensional lattice QED model using a VQE algorithm. **a)** Lattice configurations in $d = 1$ (left) and $d = 2$ (right) space dimensions with boundary conditions as indicated by red arrows. Such conditions might be induced by (anti-)particles sitting outside of the lattice. **b)** The particle number N of the ground state is shown as a function of varying mass m for $d = 1$, resulting from an ideal VQE algorithm (red dots) and from a hardware simulation on a superconducting quantum device (blue triangles). The resources reduce to 5 qubits, 16 cnots and 3 variational parameters. We observe the string-breaking phenomenon in form of a phase transition from a particle-antiparticle pair (left inset) to a flux-tube configuration (right inset) at critical mass $m_c = 3$. **c)** The electric flux L_i for each lattice link i and the particle number N (lower-right inset) of the ground state are plotted as a function of varying mass m for $d = 2$, resulting from an ideal VQE algorithm. Only one exact curve (black) for the electric flux is shown since the ground state flux configurations on each link coincide. The string-breaking phase transition is found to occur at a critical mass $m_c = 2.5$. In the small-mass regime, the ground state corresponds to a symmetric superposition of two particle-antiparticle pair configurations in which the flux-tube can pass along two distinct paths (upper-left inset) of the plaquette.

ated by combining pieces of the Yang-Mills Hamiltonian \hat{H}_{YM} in Eq. (1) which commute with the Gauss law operators. These pieces can be promoted to the following parametrized terms:

$$\text{Mass-like} \quad \hat{\psi}_x^\dagger A(\boldsymbol{\theta}) \hat{\psi}_x \quad (3)$$

$$\text{Left-hopp-like} \quad \hat{\psi}_x^\dagger A(\boldsymbol{\theta}) \hat{U}_{(x,k)} \hat{\psi}_{x+k} \quad (4)$$

$$\text{Right-hopp-like} \quad \hat{\psi}_{x+k}^\dagger A(\boldsymbol{\theta}) \hat{U}_{(x,k)}^\dagger \hat{\psi}_x \quad (5)$$

$$\text{Left-flux-like} \quad \Lambda(\boldsymbol{\theta}) \sum_{\alpha} (\hat{L}_{(x,k)}^{\alpha})^2 \quad (6)$$

$$\text{Right-flux-like} \quad \Lambda(\boldsymbol{\theta}) \sum_{\alpha} (\hat{R}_{(x,k)}^{\alpha})^2 \quad (7)$$

$$\text{String-like} \quad \hat{\psi}_x^\dagger A(\boldsymbol{\theta}) \hat{U}_1 \hat{U}_2 \cdots \hat{U}_l \hat{\psi}_{x+l} \quad (8)$$

$$\text{Loop-like} \quad \Lambda(\boldsymbol{\theta}) \text{Tr} \left(\prod_{l \in \mathcal{C}} \hat{U}_l \right) \quad (9)$$

where $\Lambda(\boldsymbol{\theta})$ is a real scalar, and the *coupling matrix* $A(\boldsymbol{\theta})$ is an arbitrary $n_{\text{spinor}} \times n_{\text{spinor}}$ matrix that mixes the spinor components of the fermionic matter fields [53]. We implicitly sum over all color and spinor indices b, c and i, j . For example, Eq. (4) would more explicitly read $\sum_{i,j,b,c} (\hat{\psi}_x^\dagger)_{b,i} A(\boldsymbol{\theta})_{ij} (\hat{U}_{(x,k)})_{bc} (\hat{\psi}_{x+k})_{c,j}$. In the *string-like* term, the link variables \hat{U}_n can be chosen such

that their product forms an arbitrary path which connects the lattice sites x and $x+l$ along lattice edges. The set \mathcal{C} in the loop-like term denotes an ordered sequence of links that form a loop. We then construct a gauge invariant unitary variational form $\hat{U}(\boldsymbol{\theta})$ by defining $\hat{U}(\boldsymbol{\theta}) = \prod_k \exp \left(i [\hat{F}_k(\boldsymbol{\theta}) + \hat{F}_k^\dagger(\boldsymbol{\theta})] \right)$, where $\hat{F}_k(\boldsymbol{\theta})$ denotes any linear combination or product of the gauge invariant terms (3) – (9) [52]. In this respect, the present variational form is conceptually different from the so-called Hamiltonian variational ansatz introduced in [54], inspired by a trotterization of an annealing process.

Results and discussion. In the following, we specialize to the $U(1)$ case of the Yang-Mills model (1), and study the phenomenon of string breaking in (1+1)- and (2+1)-dimensional lattice QED which is reminiscent of *confinement* in QCD. First, we aim to represent the groundstates in different (fermionic) mass regimes using the gauge invariant trial states $|\phi(\boldsymbol{\theta})\rangle = \hat{U}(\boldsymbol{\theta}) |\phi_{\text{init}}\rangle$. Here, the initial state $|\phi_{\text{init}}\rangle$ is chosen as the gauge invariant bare vacuum state configuration with zero particles on the lattice sites. The lattice configurations and open boundary conditions are assumed as sketched in Fig. 1 a).

For our specific model we use Wilson fermions with $r = a = 1$, $g = 5 - d$ and we adopt the Quantum

Link Model approach [26] for the gauge fields with a minimal truncation value of $S = 0.5$ and a background electric field $\theta = 0.5$. This choice encompasses either a single positive or a vanishing electric flux on each link. Note that due to our specific choice of the boundary conditions, this truncation does not affect the quality of the ground-state predictions (see Supplementary Material [44]). To approximate the ground state, we employ the variational quantum eigensolver (VQE) algorithm [37, 50] on the circuit variables θ , for each value of the varying mass m (see Fig. 1).

Starting with the $d = 1$ dimensional case, we define a specific family of gauge-invariant unitaries by

$$\hat{U}(\{\theta_x^k\}, \{\lambda_x\}) = \prod_{x,k} \exp \left[i \left(\hat{\psi}_x^\dagger A(\theta_x^k) \hat{U}_{(x,k)} \hat{\psi}_{x+k} + \text{h.c.} \right) \right] \cdots \prod_x \exp \left[i \left(\hat{\psi}_x^\dagger B(\lambda_x) \hat{\psi}_x \right) \right] \quad (10)$$

while in the $d = 2$ case, the variational form (10) is extended by string-like terms $\hat{S}(\theta)$ of the form

$$\hat{S}(\{\theta_x^{k,l}\}) = \prod_{x,k,l} \exp \left[i \left(S_{kl} + S_{kl}^\dagger \right) \right] \cdots \prod_{x,k,l} \exp \left[i \left(S_{kl} + S_{kl}^\dagger \right) \left(S_{lk} + S_{lk}^\dagger \right) \right], \quad (11)$$

where $k, l > 0$ and $S_{kl} = \hat{\psi}_x^\dagger A(\theta_x^{k,l}) \hat{U}_{(x,k)} \hat{U}_{(x+k,l)} \hat{\psi}_{x+k+l}$ as to provide longer range explicit correlations. The coupling matrices are defined as $A(\theta) = ((0,0), (\theta,0))$ and $B(\lambda) = ((0,0), (0,\lambda))$. Finally, the variational operator $\hat{U}(\theta)$ is translated into a quantum circuit by means of a Trotter approximation [55, 56] with one single Trotter step, and by using the Jordan-Wigner fermion-to-qubit mapping and a logarithmic encoding of the gauge field operators [26].

The results of the variational simulation [57] are shown in Fig. 1 b) and c) for $d = 1$ and $d = 2$ dimensions, respectively. The best run (i.e., the one with the lowest groundstate energy E_0) out of five independent VQE optimization trials (each with randomly chosen initial parameters θ) is plotted. In fact, due to the small difference between the groundstate and the first excited state in the $d = 2$ case (as explained below), more optimization trials in the VQE algorithm were needed to obtain the true groundstate. We identify the *phase transition* from a particle-antiparticle state to a single flux-string state by plotting the particle number $N = \langle \hat{N} \rangle = \sum_x \langle \hat{\psi}_x \hat{\psi}_x + \mathbb{I} \rangle$ as a function of the mass parameter m . In $d = 2$ dimensions, we further plot the expectation value of the electric flux $L = \langle \hat{E}_{(x,k)} + \theta \rangle$ for each link in Fig. 1 c). In this last case, for small m , the groundstate is a superposition of states where the flux is traversing the plaquette through two possible paths (see inset in Fig. 1 c). The degeneracy between the symmetric and antisymmetric combination

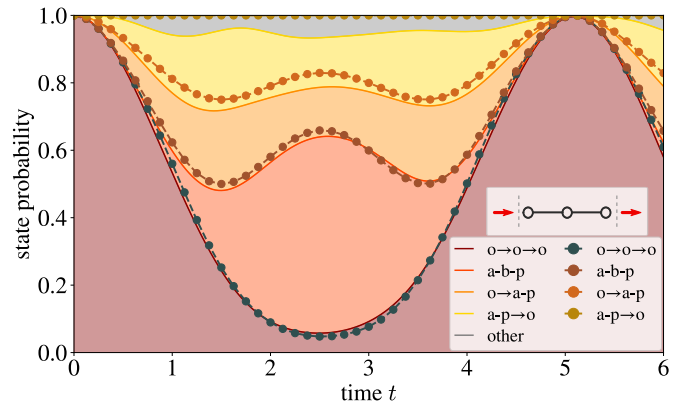


FIG. 2. State representability of the variational trial states in the real-time dynamics of a one-dimensional lattice with three sites and open boundary conditions (as sketched in the inset). The chosen model parameters read $r = a = 1$, $g = 3$, $m = 1$, $S = \theta = 0.5$. The probabilities of the different state configurations are shown as a function of time t for exact evolution (solid lines) and for the optimized trial states (dotted lines). Symbols: ‘o’: empty site, ‘a’: anti-particle, ‘p’: particle; ‘b’: particle/anti-particle pair, ‘-’: no flux line, ‘→’: flux line to the right.

of the two paths is broken by the presence of the small (as $g^2 \gg 1/g^2$) but sizable plaquette term in the Hamiltonian (see Eq. (1)).

We also perform, as a proof-of-principle, calculations on hardware for the $d = 1$ model using the *ibmq_vigo* device provided by IBM Quantum (see Fig. 1 b). The resulting circuit features 5 qubits and 16 CNOT gates with 3 variational parameters [44]. Crucially, this strategy allows us to retrieve a qualitatively better description of the problem using much less parameters and entangling gates compared to heuristic circuit ansätze (see Supplementary Material [44]).

Finally, we investigate the state representability of the proposed ansatz for real-time dynamics using the one-dimensional lattice Hamiltonian with three sites in the small mass regime $m \ll m_c$. The model parameters are the same as for the simulations shown in Fig. 1 b) with explicit mass values $m = 1$ and $m_c = 3.5$. The trial states are constructed using the unitary (10). At each time step, we numerically maximize the overlap $|\langle \phi(\theta) | \psi(t) \rangle|^2$ between the variational trial states $|\phi(\theta)\rangle$ and the exact time-evolved state $|\psi(t)\rangle$ obtained by using the matrix representation of the time propagator. In Fig. 2, we show how the trial states can capture the correct particle number oscillation characteristic of string-breaking. These are of particular relevance in view of the possible use of the proposed circuits in variational time evolution algorithms [58]. In fact, the circuit used in this example merely requires 32 CNOT gates (a value that in the variation algorithm remains constant for every time t) and 5 variational parameters.

On the other hand, the standard Trotterization approach requires a much larger number of CNOT gates, as a single Trotter step would feature 216 CNOTS, while at least ~ 10 Trotter steps would be needed to reach an accuracy [26] comparable to the one reported in Fig. 2.

Conclusions. We introduced a general methodology to construct parametrized families of quantum circuits that preserve the gauge symmetry for $U(1)$ and Yang-Mills theories. When applied to ground-state search algorithms, the method allows for reliable variational calculations as the trial states are always constrained within the physical submanifold of the full Hilbert space, reducing therefore the number of variational parameters. The main advantages of realizing the Gauss law constraint at the circuit level, rather than as an energy penalty term [26], include: (i) the smoothness of the resulting energy landscape, which allows for faster optimizations, and (ii) a substantial decrease of the energy estimator variance [51, 59] due to the absence of the (usually large) energy penalty term (see Supplementary Material [44]). In this work we demonstrated the accuracy of the method in QED models featuring particles and fields as explicit degrees of freedom.

Going beyond ground-state simulations, we show that the proposed gauge invariant trial states can further efficiently represent quantum states originating from real-time evolution, realizing a significant reduction in circuit depth (gate count) compared to standard approaches based on the Trotterization of the time-evolution operator. We therefore anticipate the usage of the present quantum circuits in combination with variational real-time evolution algorithms [58] to reduce the computational costs associated with the simulation of the dynamics of $SU(N)$ gauge theories, such as quantum chromodynamics.

-
- [1] C. N. Yang and R. L. Mills, “Conservation of isotopic spin and isotopic gauge invariance,” *Phys. Rev.* **96**, 191–195 (1954).
- [2] M.E. Peskin and D.V. Schroeder, *An Introduction To Quantum Field Theory*, Frontiers in Physics (Avalon Publishing, 1995).
- [3] Michael Creutz, Laurence Jacobs, and Claudio Rebbi, “Monte carlo computations in lattice gauge theories,” *Physics Reports* **95**, 201–282 (1983).
- [4] Pietro Silvi, Enrique Rico, Tommaso Calarco, and Simone Montangero, “Lattice gauge tensor networks,” *New Journal of Physics* **16**, 103015 (2014).
- [5] Pietro Silvi, Enrique Rico, Marcello Dalmonte, Ferdinand Tschirsich, and Simone Montangero, “Finite-density phase diagram of a $(1 + 1) - d$ non-abelian lattice gauge theory with tensor networks,” *Quantum* **1**, 9 (2017).
- [6] Pietro Silvi, Yannick Sauer, Ferdinand Tschirsich, and Simone Montangero, “Tensor network simulation of an $su(3)$ lattice gauge theory in 1d,” *Phys. Rev. D* **100**, 074512 (2019).
- [7] T. Pichler, M. Dalmonte, E. Rico, P. Zoller, and S. Montangero, “Real-time dynamics in $u(1)$ lattice gauge theories with tensor networks,” *Phys. Rev. X* **6**, 011023 (2016).
- [8] M. Dalmonte and S. Montangero, “Lattice gauge theory simulations in the quantum information era,” *Contemp. Phys.* **57**, 388–412 (2016), arXiv:1602.03776 [cond-mat.quant-gas].
- [9] Mattia Dalla Brida, Patrick Fritzsche, Tomasz Korzec, Alberto Ramos, Stefan Sint, and Rainer Sommer (ALPHA Collaboration), “Determination of the qcd Λ parameter and the accuracy of perturbation theory at high energies,” *Phys. Rev. Lett.* **117**, 182001 (2016).
- [10] Simone Montangero, *Introduction to tensor network methods : numerical simulations of low-dimensional many-body quantum systems* (Springer Verlag, 2018).
- [11] M. Tanabashi *et al.* (Particle Data Group), “Review of particle physics,” *Phys. Rev. D* **98**, 030001 (2018).
- [12] Matthias Troyer and Uwe-Jens Wiese, “Computational complexity and fundamental limitations to fermionic quantum monte carlo simulations,” *Phys. Rev. Lett.* **94**, 170201 (2005).
- [13] Mari Carmen Bañuls, Krzysztof Cichy, J. Ignacio Cirac, Karl Jansen, and Stefan Kühn, “Efficient basis formulation for $(1 + 1)$ -dimensional $su(2)$ lattice gauge theory: Spectral calculations with matrix product states,” *Phys. Rev. X* **7**, 041046 (2017).
- [14] John Kogut and Leonard Susskind, “Hamiltonian formulation of wilson’s lattice gauge theories,” *Phys. Rev. D* **11**, 395–408 (1975).
- [15] Mari Carmen Banuls, Rainer Blatt, Júlia Catani, Alessio Celi, Juan Ignacio Cirac, Marcello Dalmonte, Leonardo Fallani, K. Jansen, Maciej Lewenstein, Simone Montangero, Christine A. Muschik, Benni Reznik, Eduardo Rico, Luca Tagliacozzo, Karel Van Acoleyen, Frank Verstraete, U.-J. Wiese, Mtd Wingate, Jan Zakrzewski, and Peter Zoller, “Simulating lattice gauge theories within quantum technologies,” arXiv:1911.00003 (2019).
- [16] Simone Notarnicola, Mario Collura, and Simone Montangero, “Real-time-dynamics quantum simulation of $(1 + 1)$ -dimensional lattice qed with rydberg atoms,” *Phys. Rev. Research* **2**, 013288 (2020).
- [17] Yoshihito Kuno, Shinya Sakane, Kenichi Kasamatsu, Ikuro Ichinose, and Tetsuo Matsui, “Quantum simulation of $(1 + 1)$ -dimensional $u(1)$ gauge-higgs model on a lattice by cold bose gases,” *Phys. Rev. D* **95**, 094507 (2017).
- [18] A. Mezzacapo, E. Rico, C. Sabín, I. L. Egusquiza, L. Lamata, and E. Solano, “Non-abelian $su(2)$ lattice gauge theories in superconducting circuits,” *Phys. Rev. Lett.* **115**, 240502 (2015).
- [19] Bing Yang, Hui Sun, Robert Ott, Han-Yi Wang, Thorsten V Zache, Jad C Halimeh, Zhen-Sheng Yuan, Philipp Hauke, and Jian-Wei Pan, “Observation of gauge invariance in a 71-site bose–hubbard quantum simulator,” *Nature* **587**, 392–396 (2020).
- [20] Tim Byrnes and Yoshihisa Yamamoto, “Simulating lattice gauge theories on a quantum computer,” *Phys. Rev. A* **73**, 022328 (2006).
- [21] Ruben S Andrist, Helmut G Katzgraber, H Bombin, and M A Martin-Delgado, “Tricolored lattice gauge theory

- with randomness: fault tolerance in topological color codes,” *New Journal of Physics* **13**, 083006 (2011).
- [22] D. Banerjee, M. Bögli, M. Dalmonte, E. Rico, P. Stebler, U.-J. Wiese, and P. Zoller, “Atomic quantum simulation of $U(n)$ and $SU(n)$ non-abelian lattice gauge theories,” *Phys. Rev. Lett.* **110**, 125303 (2013).
- [23] Dayou Yang, Gouri Shankar Giri, Michael Johanning, Christof Wunderlich, Peter Zoller, and Philipp Hauke, “Analog quantum simulation of $(1+1)$ -dimensional lattice qed with trapped ions,” *Phys. Rev. A* **94**, 052321 (2016).
- [24] Esteban A. Martinez, Christine A. Muschik, Philipp Schindler, Daniel Nigg, Alexander Erhard, Markus Heyl, Philipp Hauke, Marcello Dalmonte, Thomas Monz, Peter Zoller, and Rainer Blatt, “Real-time dynamics of lattice gauge theories with a few-qubit quantum computer,” *Nature* **534**, 516 EP – (2016).
- [25] C. Kokail, C. Maier, R. van Bijnen, T. Brydges, M. K. Joshi, P. Jurcevic, C. A. Muschik, P. Silvi, R. Blatt, C. F. Roos, and P. Zoller, “Self-verifying variational quantum simulation of lattice models,” *Nature* **569**, 355–360 (2019).
- [26] Simon V. Mathis, Guglielmo Mazzola, and Ivano Tavernelli, “Toward scalable simulations of lattice gauge theories on quantum computers,” *Phys. Rev. D* **102**, 094501 (2020).
- [27] Henry Lamm, Scott Lawrence, and Yukari Yamauchi (NuQS Collaboration), “General methods for digital quantum simulation of gauge theories,” *Phys. Rev. D* **100**, 034518 (2019).
- [28] Jad C. Halimeh and Philipp Hauke, “Reliability of lattice gauge theories,” *Phys. Rev. Lett.* **125**, 030503 (2020).
- [29] Jad C. Halimeh, Robert Ott, Ian P. McCulloch, Bing Yang, and Philipp Hauke, “Robustness of gauge-invariant dynamics against defects in ultracold-atom gauge theories,” *Phys. Rev. Research* **2**, 033361 (2020).
- [30] Barak Bringoltz, “Volume dependence of two-dimensional large- n qed with a nonzero density of baryons,” *Phys. Rev. D* **79**, 105021 (2009).
- [31] P. Sala, T. Shi, S. Kühn, M. C. Bañuls, E. Demler, and J. I. Cirac, “Variational study of $u(1)$ and $su(2)$ lattice gauge theories with gaussian states in $1+1$ dimensions,” *Phys. Rev. D* **98**, 034505 (2018).
- [32] Erez Zohar and J. Ignacio Cirac, “Removing staggered fermionic matter in $u(n)$ and $su(n)$ lattice gauge theories,” *Phys. Rev. D* **99**, 114511 (2019).
- [33] David B. Kaplan and Jesse R. Stryker, “Gauss’s law, duality, and the hamiltonian formulation of $u(1)$ lattice gauge theory,” *Phys. Rev. D* **102**, 094515 (2020).
- [34] Jesse R. Stryker, “Oracles for gauss’s law on digital quantum computers,” *Phys. Rev. A* **99**, 042301 (2019).
- [35] Timo Felser, Pietro Silvi, Mario Collura, and Simone Montangero, “Two-dimensional quantum-link lattice quantum electrodynamics at finite density,” *Phys. Rev. X* **10**, 041040 (2020).
- [36] Claudine Lacroix, Philippe Mendels, and Frédéric Mila, *Introduction to frustrated magnetism: materials, experiments, theory*, Vol. 164 (Springer Science & Business Media, 2011).
- [37] Alberto Peruzzo, Jarrod McClean, Peter Shadbolt, Man-Hong Yung, Xiao-Qi Zhou, Peter J. Love, Alán Aspuru-Guzik, and Jeremy L. O’Brien, “A variational eigenvalue solver on a photonic quantum processor,” *Nature Communications* **5**, 4213 (2014).
- [38] Michael A. Nielsen and Isaac L. Chuang, *Quantum Computation and Quantum Information: 10th Anniversary Edition* (Cambridge University Press, 2010).
- [39] Daniel S Abrams and Seth Lloyd, “Quantum algorithm providing exponential speed increase for finding eigenvalues and eigenvectors,” *Physical Review Letters* **83**, 5162 (1999).
- [40] Assuming that the initial state of interest dynamics is not trivially represented in the computational basis.
- [41] Christian Schweizer, Fabian Grusdt, Moritz Berngruber, Luca Barbiero, Eugene Demler, Nathan Goldman, Immanuel Bloch, and Monika Aidelsburger, “Floquet approach to \mathbb{Z}_2 lattice gauge theories with ultracold atoms in optical lattices,” *Nature Physics* **15**, 1168–1173 (2019).
- [42] Erez Zohar, J. Ignacio Cirac, and Benni Reznik, “Quantum simulations of gauge theories with ultracold atoms: Local gauge invariance from angular-momentum conservation,” *Phys. Rev. A* **88**, 023617 (2013).
- [43] U.-J. Wiese, “Ultracold quantum gases and lattice systems: quantum simulation of lattice gauge theories,” *Annalen der Physik* **525**, 777–796 (2013).
- [44] See Supplemental Material for more details concerning the quantum computing implementation of the LGT theory, the trial states, the quantum circuits, additional results, and benchmarks.
- [45] John B. Kogut, “The lattice gauge theory approach to quantum chromodynamics,” *Rev. Mod. Phys.* **55**, 775–836 (1983).
- [46] T V Zache, F Hebenstreit, F Jendrzejewski, M K Oberthaler, J Berges, and P Hauke, “Quantum simulation of lattice gauge theories using wilson fermions,” *Quantum Science and Technology* **3**, 034010 (2018).
- [47] R. Brower, S. Chandrasekharan, and U.-J. Wiese, “Qcd as a quantum link model,” *Phys. Rev. D* **60**, 094502 (1999).
- [48] Lena Funcke, Karl Jansen, and Stefan Kühn, “Topological vacuum structure of the schwinger model with matrix product states,” *Phys. Rev. D* **101**, 054507 (2020).
- [49] Peter Orland and Daniel Rohrlich, “Lattice gauge magnets: Local isospin from spin,” *Nuclear Physics B* **338**, 647 – 672 (1990).
- [50] Jarrod R McClean, Jonathan Romero, Ryan Babbush, and Alán Aspuru-Guzik, “The theory of variational hybrid quantum-classical algorithms,” *New Journal of Physics* **18**, 023023 (2016).
- [51] Abhinav Kandala, Antonio Mezzacapo, Kristan Temme, Maika Takita, Markus Brink, Jerry M. Chow, and Jay M. Gambetta, “Hardware-efficient variational quantum eigensolver for small molecules and quantum magnets,” *Nature* **549**, 242–246 (2017).
- [52] Note that due to the linearity and the product rule $[AB, C] = A[B, C] + [A, C]B$ of the commutator for arbitrary operators A , B and C , it follows that any linear combination or product of gauge invariant terms will remain gauge invariant.
- [53] We allow the mixing of the spinor components since these spinors are all affected in the same manner under a gauge transformation and a mixing does not change the gauge invariance properties of these terms. On the other hand, mixing the color components in an arbitrary manner would destroy the gauge symmetry of these terms.
- [54] Dave Wecker, Matthew B. Hastings, and Matthias Troyer, “Progress towards practical quantum variational algorithms,” *Phys. Rev. A* **92**, 042303 (2015).

- [55] H. F. Trotter, “On the product of semi-groups of operators,” *Proceedings of the American Mathematical Society* **10**, 545–551 (1959).
- [56] Masuo Suzuki, “Generalized trotter’s formula and systematic approximants of exponential operators and inner derivations with applications to many-body problems,” *Communications in Mathematical Physics* **51**, 183–190 (1976).
- [57] Héctor Abraham, Ismail Yunus Akhalwaya, Gadi Aleksandrowicz, *et al.*, “Qiskit: An open-source framework for quantum computing,” (2019).
- [58] Xiao Yuan, Suguru Endo, Qi Zhao, Ying Li, and Simon C. Benjamin, “Theory of variational quantum simulation,” *Quantum* **3**, 191 (2019).
- [59] Sergey Bravyi, Jay M. Gambetta, Antonio Mezzacapo, and Kristan Temme, “Tapering off qubits to simulate fermionic hamiltonians,” arXiv:1701.08213v1 (2017).
- [60] Simon V. Mathis, *Simulation of U(1)-lattice gauge theories on digital quantum computers*, Master’s thesis, ETH Zurich (2019).
- [61] One might expect the groundstate energy for vanishing hopping term in the small mass regime $m \ll m_c$ to be equal to zero since both the electric field term and the mass vanish for the gauge invariant particle-antiparticle pair state. However, the small negative energy contribution that is visible in the left graph originates from the Wilson term which contains a hopping like term proportional to r and which was not set to zero.
- [62] Note that the explicit gauge invariant variational form (S19) that is used in our simulations consists of four Pauli strings as a result of the Jordan-Wigner mapping which all pairwise commute. Thus, there is no Trotter approximation error in our simulations.

Supplementary Material: Gauge invariant quantum circuits for $U(1)$ and Yang-Mills lattice gauge theories

THE YANG-MILLS LATTICE MODEL

Here, we shortly summarize all the relevant operators and their respective relations that have to be taken into account in a simulation of a lattice model that respects the continuous gauge symmetry of a Yang-Mills gauge theory and which reproduces the correct dynamics of such a theory in the continuum limit.

In this work, the Yang-Mills theory is formulated on a d -dimensional discrete spatial lattice with spacing a , and the time component is kept as a continuous parameter. The (single flavor) fermionic particles reside on the lattice sites x , while the gauge fields live on the links (x, k) in between. The Yang-Mills Hamiltonian in the temporal gauge reads

$$\begin{aligned} \hat{H}_{\text{YM}} &= \hat{H}_{\text{hopp}} + \hat{H}_{\text{mass}} + \hat{H}_{\text{wilson}} + \hat{H}_{\text{elec}} + \hat{H}_{\text{plaq}} \\ &= \sum_{\text{sites}} \sum_k \frac{1}{2a} \left(\hat{\psi}_x [i\gamma^k + r] \hat{U}_{(x,k)} \hat{\psi}_{x+k} + \text{h.c.} \right) + \sum_{\text{sites}} \left(m + \frac{rd}{a} \right) \hat{\psi}_x \hat{\psi}_x \\ &\quad + \frac{g^2 a^{2-d}}{4} \sum_{\text{links}} \sum_{\alpha} \left((\hat{L}_{(x,k)}^{\alpha})^2 + (\hat{R}_{(x,k)}^{\alpha})^2 \right) - \frac{a^{d-4}}{2g^2} \sum_{\text{plaq.}} \text{Tr} \left(\hat{U}_{\square} + \hat{U}_{\square}^{\dagger} \right) \end{aligned} \quad (\text{S1})$$

and mainly consists of five contributing terms. The first term \hat{H}_{hopp} in (S1) is called **hopping term** and describes the hopping of the fermionic particles between adjacent lattices sites. The second term \hat{H}_{mass} is the **mass term** that corresponds to the mass m that is carried by the fermionic particles. The **Wilson term** \hat{H}_{wilson} is introduced via the parameter r and acts as a regulator to avoid the fermion doubling problem. The last two terms in the Hamiltonian introduce the dynamics of the bosonic gauge fields. The **electric term** \hat{H}_{elec} counts the electric color flux on a link and is built up of the left and right gauge generators \hat{L} and \hat{R} . The **plaquette term** \hat{H}_{plaq} corresponds to the magnetic field energy contribution and consists of plaquette operators of the form

$$\hat{U}_{\square} \equiv \hat{U}_{(x,kl)} = \hat{U}_{(x,k)} \hat{U}_{(x+k,l)} \hat{U}_{(x+l,k)}^{\dagger} \hat{U}_{(x,l)}^{\dagger}. \quad (\text{S2})$$

The bare coupling constant parameter g specifies the interaction strength between the gauge- and matter fields, and can be interpreted as the fundamental unit of the color electric charge.

The quantities $\hat{\psi}$ and $\hat{\psi}$ act as creation- and annihilation operators of fermionic particles, respectively. These fermionic operators implicitly carry spinor- and color component indices,

$$\hat{\psi}_x^{b,j} \begin{cases} \text{spinor indices} & i, j, \dots \in \{1, \dots, 2^{\lceil d/2 \rceil}\} \\ \text{color indices} & b, c, \dots \in \{1, \dots, \dim(R)\} \\ \text{spatial lattice indices} & x, y \in \Gamma \end{cases}$$

where $\dim(R)$ denotes the dimension of the representation R of the corresponding gauge group G . For example, in the case of $G = SU(N)$ in the fundamental representation, we have $\dim(R) = N$. Note that whenever the spinor- and color indices are suppressed (such as in the Hamiltonian H_{YM}), it is implicitly summed over all these indices. The fermionic operators satisfy the anticommutation relations

$$\left\{ \hat{\psi}_x^{b,i}, \hat{\psi}_y^{\dagger c,j} \right\} = \delta_{xy} \delta_{bc} \delta_{ij}, \quad \left\{ \hat{\psi}_x^{b,i}, \hat{\psi}_y^{c,j} \right\} = \left\{ \hat{\psi}_x^{\dagger b,i}, \hat{\psi}_y^{\dagger c,j} \right\} = 0. \quad (\text{S3})$$

The continuous gauge group G is generated by elements T^α such that

$$[T^\alpha, T^\beta] = i f^{\alpha\beta\gamma} T^\gamma \quad \alpha, \beta, \gamma \in \{1, \dots, \dim(G)\} \quad (\text{S4})$$

where $f^{\alpha\beta\gamma}$ denote the totally antisymmetric structure constants which encode the structure of the group G . The generators are usually expressed in the fundamental representation.

The link variables $\hat{U}_{(x,k)}$ on a link (x,k) have the same structure as the group generators T^α : They are $\dim(R) \times \dim(R)$ dimensional matrices whose entries $(\hat{U}_{(x,k)})_{mn}$ are operators that act on the link Hilbert space. The conjugate link variables $\hat{L}_{(x,k)}^\alpha$ and $\hat{R}_{(x,k)}^\alpha$ are defined through the relations

$$\left[\hat{L}_{(x,k)}^\alpha, (\hat{U}_{(x,k)})_{mn} \right] = (T^\alpha \hat{U}_{(x,k)})_{mn}, \quad \left[\hat{R}_{(x,k)}^\alpha, (\hat{U}_{(x,k)})_{mn} \right] = (\hat{U}_{(x,k)} T^\alpha)_{mn} \quad (\text{S5})$$

$$\left[\hat{L}_{(x,k)}^\alpha, \hat{L}_{(x,k)}^\beta \right] = -i f^{\alpha\beta\gamma} \hat{L}_{(x,k)}^\gamma, \quad \left[\hat{R}_{(x,k)}^\alpha, \hat{R}_{(x,k)}^\beta \right] = i f^{\alpha\beta\gamma} \hat{R}_{(x,k)}^\gamma, \quad \left[\hat{L}_{(x,k)}^\alpha, \hat{R}_{(x,k)}^\beta \right] = 0 \quad (\text{S6})$$

while all operators assigned to different links commute with each other. The variables $\hat{L}_{(x,k)}^\alpha$ and $\hat{R}_{(x,k)}^\alpha$ are associated with the left end and the right end of a link (x,k) , respectively.

The Gauss law operators are defined by

$$\hat{G}_x^\alpha = \sum_k \left(\hat{L}_{(x,k)}^\alpha - \hat{R}_{(x-k,k)}^\alpha \right) - \hat{\psi}_x^\dagger T^\alpha \hat{\psi}_x \quad (\text{S7})$$

and they specify the gauge-invariant states $|\phi_{\text{phys}}\rangle$ that span the physical Hilbert space via

$$\hat{G}_x^\alpha |\phi_{\text{phys}}\rangle = 0, \quad \left[\hat{H}_{\text{YM}}, \hat{G}_x^\alpha \right] = 0 \quad \forall x \in \Gamma \text{ and } \alpha \in \{1, \dots, \dim(G)\}. \quad (\text{S8})$$

Finally, let us characterize the Hilbert space \mathcal{H}_{YM} on which the Hamilton operator \hat{H}_{YM} acts. On each lattice site x , the fermionic particles span a Hilbert space $\mathcal{H}_x^{\text{fermi}}$ of dimension

$$\dim(\mathcal{H}_x^{\text{fermi}}) = 2^{\mathbf{q}}, \quad \mathbf{q} = 2^{\lceil d/2 \rceil} \cdot \dim(R) \quad (\text{S9})$$

where \mathbf{q} corresponds to the total number of fermionic modes which are either occupied or unoccupied.

On each link (x,k) , the bosonic gauge field variables act on a Hilbert space

$$\mathcal{H}_{(x,k)}^{\text{gauge}} = L^2(G), \quad \dim(\mathcal{H}_{(x,k)}^{\text{gauge}}) = \infty \quad (\text{S10})$$

which is infinite dimensional due to the continuous nature of the gauge group G . For this reason, the link Hilbert spaces have to be truncated in order to be simulated [S15, S26, S47, S49].

The total Hilbert space is then given as a tensor product of all the single spaces on the sites and links of the lattice,

$$\mathcal{H}_{\text{YM}} = \bigotimes_{x,k} \mathcal{H}_x^{\text{fermi}} \otimes \mathcal{H}_{(x,k)}^{\text{gauge}} \quad (\text{S11})$$

and the physical states $|\phi_{\text{phys}}\rangle$ span the physical Hilbert subspace $\mathcal{H}^{\text{phys}} \subset \mathcal{H}_{\text{YM}}$.

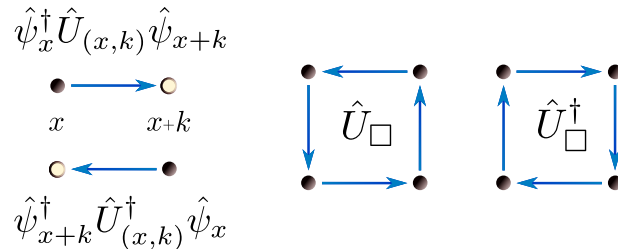


FIG. S1. Graphical illustration of the hopping terms $\hat{\psi}^\dagger \hat{U} \hat{\psi}$ and the plaquette terms \hat{U}_\square plus their hermitian conjugates on a lattice.

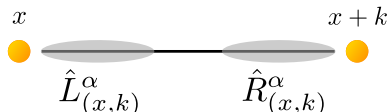


FIG. S2. Illustration of a non-abelian link. The coloured left operators $\hat{L}_{(x,k)}^\alpha$ and right operators $\hat{R}_{(x,k)}^\alpha$ are independent variables that are assigned to the left end and the right end of a link (x, k) , respectively.

Enforcing the Gauss law

Once the Yang-Mills Hamiltonian has been mapped to a finite qubit system, one can analyse properties like its spectrum or the real-time evolution that it generates. However, the Hamiltonian acts on a large Hilbert containing all possible matter and gauge field states, especially also the unphysical states that are not gauge invariant. This is a result of fixing the temporal gauge which is necessary in the canonical quantization of the Yang-Mills theory and gives rise to the Gauss law constraints (S8) that take the form $\hat{G}_x^\alpha |\phi_{\text{phys}}\rangle = 0$ in a discrete lattice formulation of the theory.

When studying the spectrum of the Yang-Mills Hamiltonian in a variational quantum simulation for example, we have to restrict ourselves to the physically relevant Hilbert space with gauge-invariant states $|\phi_{\text{phys}}\rangle$ in order to obtain the correct physical energy spectrum.

For simulations of the real-time evolution on the other hand, when starting with a gauge invariant initial state $|\phi_{\text{phys}}(0)\rangle$, then the time-evolved state $|\phi_{\text{phys}}(t)\rangle$ at time t should in principle still be gauge invariant since the Gauss law constraints are constants of motion, $[\hat{G}_x^\alpha, \hat{H}_{\text{YM}}] = 0$. For this reason, in principle there would be no need to externally enforce the Gauss law constraint. Nevertheless, errors that kick the state out of the physical Hilbert space $\mathcal{H}^{\text{phys}}$ can occur in practice due to the Trotter approximation [S55, S56] of the time-evolution operator or from quantum hardware noise.

Note that in $d = 1$, the Gauss law constraint can be directly incorporated in the Hamiltonian where the gauge fields are effectively removed [S24, S30, S31]. In this case, one works in a reduced Hilbert space where the Gauss law constrained is automatically fulfilled. However, such a process is not scalable to arbitrary space dimensions d and thus, it is not clear how to restrict oneself to the physical Hilbert space of states for $d > 1$.

In these cases, the Gauss law constraints must be separately enforced. One possible approach to do so is to insert the constraints in the Hamiltonian as additional energy penalty terms

$$\hat{H}_{\text{gauge}} = \lambda \sum_{x,\alpha} (\hat{G}_x^\alpha)^2 \quad (\text{S12})$$

for some regularization parameter λ , that effectively lift the energy of unphysical states [S26]. As a result, the low-lying energy spectrum solely comes from contributions of physical states at the expense of raising the gate complexity of the Hamiltonian.

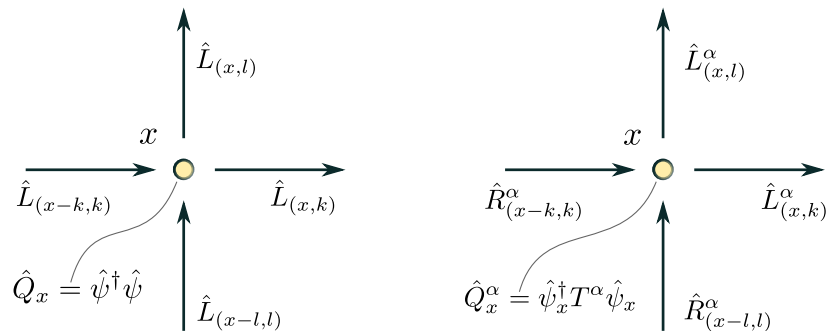


FIG. S3. Illustration of the abelian (left) and non-abelian (right) Gauss law constraint. The difference between the outgoing flux and the incoming flux on a site x equals the amount of charge that sits on that site.

PERFORMANCE OF HEURISTIC VARIATIONAL FORMS FOR $U(1)$ AND $SU(2)$ LATTICE MODELS IN 1D

In quantum field theories, the VQE [S37, S50] can be exploited to study various groundstate properties for varying model parameters. For example, one might investigate phase diagrams of Abelian and non-abelian gauge theories [S5, S6, S35] in the regime of a finite fermion density, i.e. at an unbalance between fermionic matter and antimatter, which remain inaccessible to standard Monte Carlo simulation methods due to the notorious sign-problem.

When applying the VQE algorithm to a general Yang-Mills lattice gauge theory, a challenge arises in the search for an efficient ansatz for the variational form [S60]. The reason for this challenge stems from the Gauss law constraint that determines the physical Hilbert subspace $\mathcal{H}^{\text{phys}} \subset \mathcal{H}$ which makes up an exponentially small fraction of the total Hilbert space \mathcal{H} . In our implementation (that follows the framework of Ref. [S26]), the Gauss law constraint is imposed by adding a gauge penalty term \hat{H}_{gauge} which raises the energy of the unphysical gauge-variant states. As a consequence, the gauge penalty term leads to a corrugated energy landscape (Fig. S4) whose minimum is in general hard to find for classical optimization algorithms, as was observed in [S60].

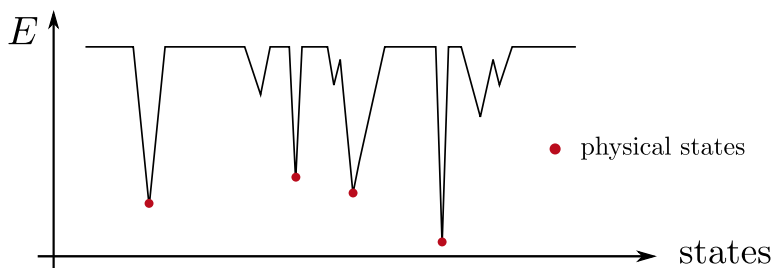
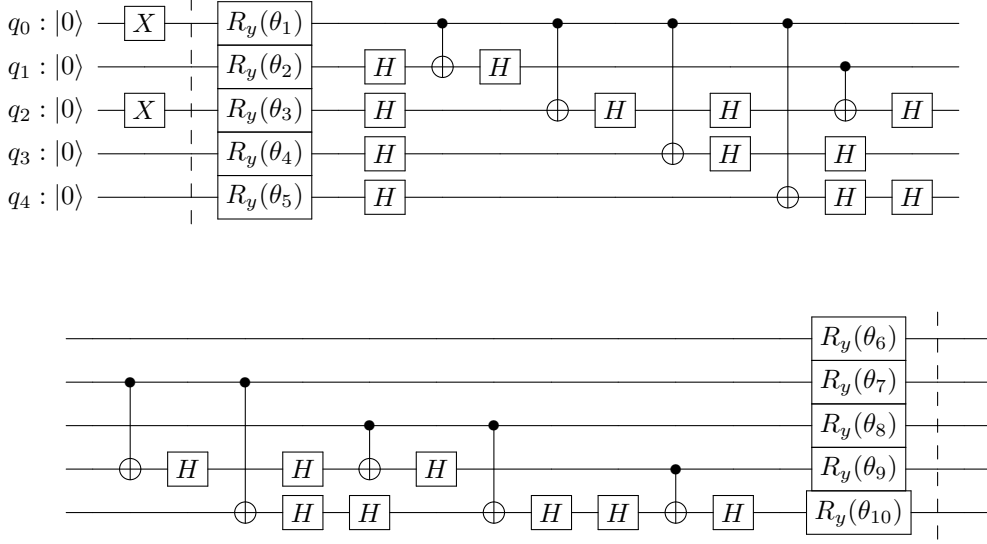


FIG. S4. Graphical illustration of the corrugated energy landscape. The gauge penalty term \hat{H}_{gauge} lifts the energy of the unphysical states in order to obtain the correct low-energy spectrum of the theory. The physical states are marked by red dots.

In order to quantitatively confirm this hypothesis, we tested the performance of the so-called R_Y and $R_Y R_Z$ variational form on a small lattice QED example in $d = 1$ dimensions for a varying mass parameter m , which is mapped to a 5-qubit system. This example is introduced in detail in the next section.

The R_Y and $R_Y R_Z$ are two standard heuristic variational forms $\hat{U}(\boldsymbol{\theta})$ that are constructed such that a wide range of states in \mathcal{H}_{YM} can be covered without taking into account the underlying structure of the corresponding physical system. To do so, these variational forms systematically entangle all of the qubits and apply parametrized rotations R_y for R_Y or R_y and R_z for $R_Y R_Z$, respectively, on each single qubit.

For sake of clarity, an example circuit for the R_Y variational form of depth 1 with *full* entanglement, i.e. where the qubits are pairwise entangled, is depicted below:



More complex trial states can be created by repeating this unit. The performance of these two variational forms is shown in Fig. S5. The relative energy difference $\Delta E = |E_{\text{vqe}} - E_0| / |E_0|$ is plotted as a function of varying mass parameter m and for increasing depth of the RY and $RYRZ$ variational forms. Each data point in the plot corresponds to a single VQE run (in statevector simulation) which achieved the lowest energy estimation E_{vqe} out of a total of 10 independent optimization runs (each starting from different randomly chosen initial parameters) for each mass value. We used the *Cobyla* optimization algorithm for the classical optimization procedure. The initial parameters $\theta^{(0)}$ were randomly chosen from a uniform distribution in $[-\pi, \pi]$ and the initial state $|\phi_{\text{init}}\rangle$ was given by the bare vacuum state, i.e. the unique gauge-invariant state with zero particles on each lattice site. For comparison, we further included the performance of the gauge-invariant variational form

$$\hat{U}(\{\theta_x^k\}, \{\lambda_x\}) = \prod_{x,k} \exp \left[i \left(\hat{\psi}_x^\dagger A(\theta_x^k) \hat{U}_{(x,k)} \hat{\psi}_{x+k} + \text{h.c.} \right) \right] \prod_x \exp \left[i \left(\hat{\psi}_x^\dagger \Lambda(\lambda_x) \hat{\psi}_x \right) \right], \quad (\text{S13})$$

where we chose

$$A(\theta_x^k) := \begin{pmatrix} 0 & 0 \\ \theta_x^k & 0 \end{pmatrix}, \quad \Lambda(\lambda_x) := \begin{pmatrix} 0 & 0 \\ 0 & \lambda_x \end{pmatrix} \quad \forall x, k. \quad (\text{S14})$$

As a consequence, the matrices $A(\theta_x^k)$ couple only the second spinor component at a site x to the first spinor component at an adjacent site $x+k$. This implies that hopping terms assigned to neighboring sites commute and thus, the products in Eq. (S13) are well-defined. Furthermore, for each site that sits in a corner of the finite lattice, there is always one spinor component that is left untouched by this variational form, allowing to effectively remove the qubits that encode these spinor components [S60]. The corresponding quantum circuit for a one-dimensional lattice system with two sites is shown in (S19).

From the results in Fig. S5 it is visible that the standard heuristic variational forms struggle to find the correct groundstate energy, resulting in a poor approximation of E_0 . Raising the circuit depth merely aggravates the performance in spite of a higher number of degrees of freedom. The origin for such large errors lies in the large regularizing coefficient $\lambda = 20$ in the gauge penalty term \hat{H}_{gauge} that leads to high energy contributions in the order of $\sim 10^2$ but which is needed to fix the correct low-lying gauge-invariant energy spectrum. Furthermore, it was observed that the performance of the standard variational forms greatly depended on the initial set of parameters $\theta^{(0)}$. Therefore, these standard variational form ansätze are not promising for larger system sizes and non-abelian gauge theories.

In contrast, the gauge-invariant variational form clearly outperforms the standard heuristic ansätze by one or two orders of magnitude. At the same time, it requires much less parameter degrees of freedom which is beneficial for the classical optimization procedure, even for larger sizes of the physical system.

We further tested the performance of the standard heuristic RY variational form on a $d = 1$ dimensional $SU(2)$ gauge theory model where the Gauss law constraint is incorporated in the Hamiltonian and the gauge degrees of

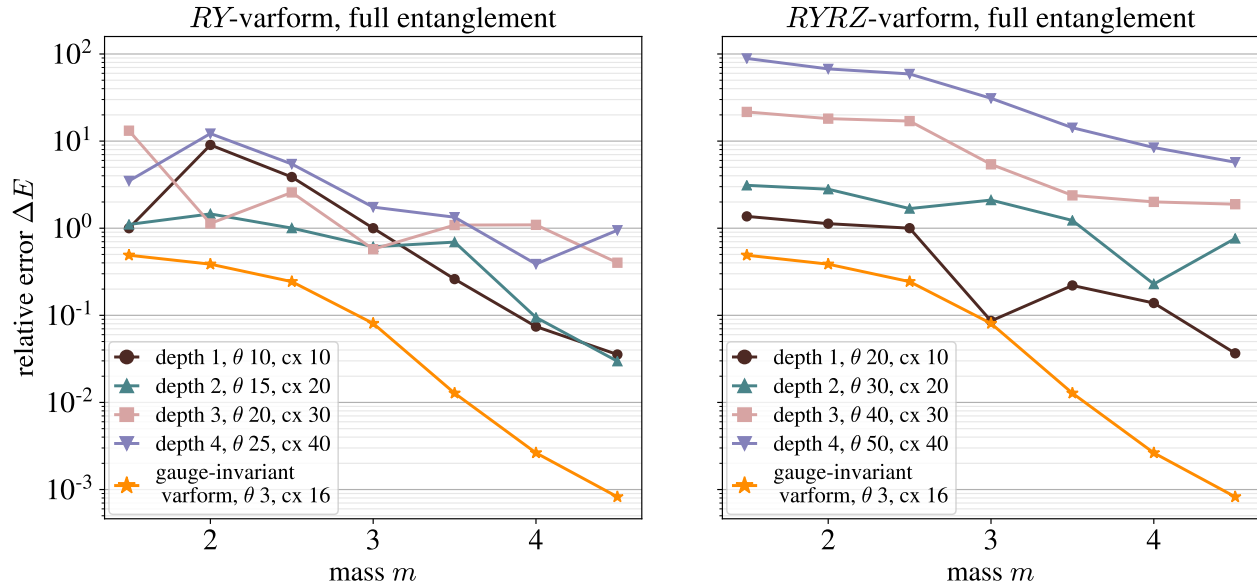


FIG. S5. Performance of the RY (left) and $RYRZ$ (right) variational form in a VQE. The relative error ΔE in energy is plotted for varying mass parameter m . Each data point corresponds to a separate VQE simulation. The " θ " denotes the number of parameters in the variational form while " cx " stands for the count of $CNOT$ gates in the corresponding circuit.

freedom are effectively erased [S31]. Since the the Hilbert space of this model only contains gauge invariant states, we expect the RY variational form to achieve better convergence to the groundstate energy.

The integrated $SU(2)$ model was implemented on $M = 2$ lattice sites with lattice spacing $a = 1$, Wilson parameter $r = 1$, coupling constant $g = 3$ and boundary conditions $\hat{R}_0^\alpha = 0, \forall \alpha$. The groundstate energy E_0 was examined as a function of varying (negative) mass parameter m . In the regime where $m \approx -r/a$, the model exhibits a specific type of phase transition from a bare vacuum phase with no particles to a charge-crystal phase where all lattice sites are fully occupied [S35]. Such a phase transition occurs when the prefactor $(m + r/a)$ of the mass term $\sum_n \hat{\psi}_n \hat{\psi}_n$ in the system Hamiltonian changes its sign from positive to negative since in the former case, the production of particles costs energy while in the latter case, it becomes energetically favourable to create particles pairs.

For various mass values m , we ran a separate ideal VQE for each m using the RY variational form with linear entanglement, i.e. where the qubits are not all pairwise entangled but only neighboring qubits are entangled, leading to a reduced number of $CNOT$ gates. We used the *Cobyla* optimization algorithm for the classical optimization procedure. The exact groundstate energy curve was calculated by exact diagonalization. The results are plotted in Fig. S6.

From these results, it is visible that the RY variational form shows a better performance with smaller relative errors $\Delta E = |E_{\text{vqe}} - E_0| / |E_0|$ for the integrated $SU(2)$ model than for the general scalable QED model with a gauge penalty term. However, the error increases in the regime of the phase transition, indicating the this heuristic variational form is not able to capture the essential properties of the groundstate in the region of the phase transition where the quantum fluctuations, arising from the hopping term in the system Hamiltonian, start to become significantly large.

It has further been checked that changing the linear entanglement to a full entanglement or raising the depth of the variational form did not lead to significant improvements for the overall performance.

To conclude, this short analysis corroborates the need of physically motivated and structured variational forms which respect the symmetries of the Yang-Mills theory at hand. Furthermore, note that heuristic standard variational forms are usually constructed at the qubit level and thus will depend on the exact encoding scheme for the gauge and matter field degrees of freedom.

$SU(2)$ Phase Transition (RY -varform, linear)

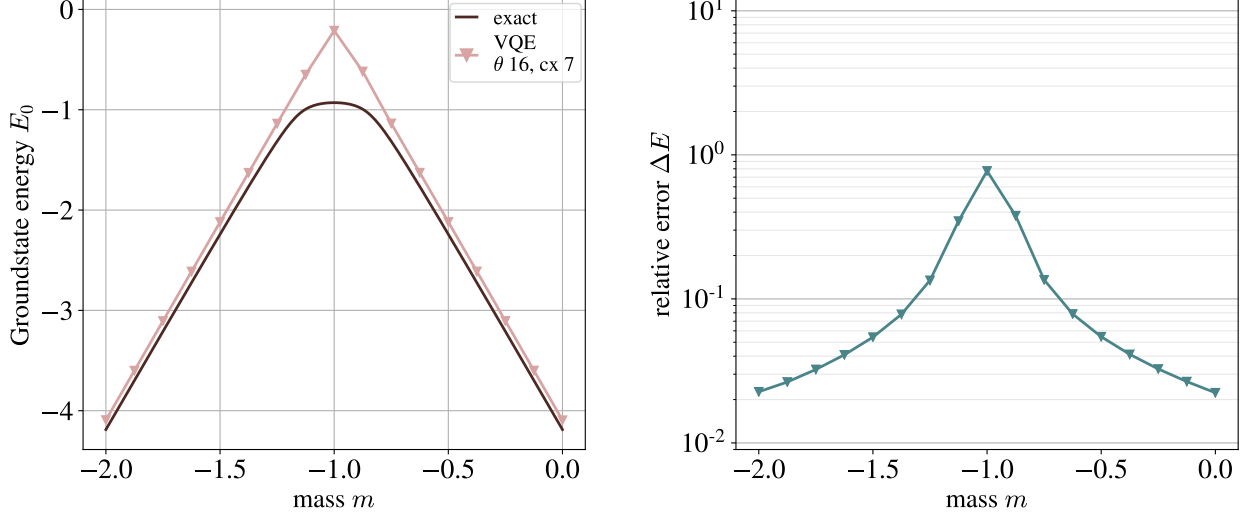


FIG. S6. Phase transition of the one-dimensional integrated $SU(2)$ model with two lattice sites and performance of the RY variational form with 16 parameters and 7 $CNOT$ gates. The groundstate energy E_0 (left) and the relative energy difference ΔE (right) are shown as a function of mass m .

LATTICE QED IN 1D ON REAL QUANTUM HARDWARE

Here we present a detailed description of the (1+1)-dimensional lattice QED system exhibiting the phenomenon of string breaking, which was simulated on a few-qubit superconducting quantum device.

The model

In the following, we consider a one dimensional lattice with $M = 2$ sites and one link with open boundary conditions. It is convenient to relabel the matter fields by $\hat{\psi}_x \rightarrow \hat{\psi}_n$, the flux operator by $\hat{L}_{(x,k)} \rightarrow \hat{L}_n$ and the link variable by $\hat{U}_{(x,k)} \rightarrow \hat{U}_n$. Recall that the QED Hamiltonian (S1) for dimension $d = 1$ including the gauge penalty term reads

$$\hat{H}_{\text{QED}} = \sum_{n=1}^{M-1} \frac{1}{2a} \left(\hat{\psi}_n [i\gamma^1 + r] \hat{U}_n \hat{\psi}_{n+1} + \text{h.c.} \right) + \sum_{n=1}^M \left(m + \frac{r}{a} \right) \hat{\psi}_n \hat{\psi}_n + \frac{g^2 a}{2} \sum_{n=1}^{M-1} \hat{L}_n^2 + \lambda \sum_{n=1}^M \hat{G}_n^2 \quad (\text{S15})$$

with $\hat{G}_n = \hat{L}_n - \hat{L}_{n-1} - \hat{\psi}_n^\dagger \hat{\psi}_n$,

where \hat{L}_0 and \hat{L}_M are not dynamical variables but are fixed by the choice of the open boundary conditions.

In addition, we allow for a non-trivial constant background electric field θ to be added to the model [S48], which is taken into account by shifting the electric flux field operator by a constant amount,

$$\hat{L}_n \rightarrow \hat{L}_n + \theta \quad \Rightarrow \quad \hat{H}_{\text{elec}} \rightarrow \frac{g^2 a}{2} \sum_{n=1}^{M-1} (\hat{L}_n + \theta)^2 \quad (\text{S16})$$

where $\theta \equiv \theta \cdot \mathbb{1}$ acts as an identity operator times a real constant. Therefore, such a background electric field effectively shifts the allowed electric flux eigenvalues m_s by an amount of θ . For example, for a spin value $S = 1.5$ in the quantum link model formulation of the Abelian gauge fields and a background electric field $\theta = 0.5$, the allowed flux eigenvalues flux eigenvalues are shifted by $m_s \in \{-1.5, -0.5, 0.5, 1.5\} \rightarrow m_s \in \{-1, 0, 1, 2\}$. As a result, the flux eigenvalues are not centered around the zero flux value anymore, thereby breaking the spatial symmetry of the physical system. Nevertheless, for certain choices of the boundary conditions or for high enough spin values S , the low-lying energy spectrum will not be affected by this shift as will be the case in the model that we are considering. On the other

hand, the background electric field will allow us to reduce the number qubits needed to store the relevant states of the model.

In our simulations, we choose the model parameters $g = 4$, $a = 1$, $r = 1$, $\lambda = 20$, the spin value $S = 0.5$ with a background electric field $\theta = 0.5$, and boundary conditions as depicted in Fig. S7.



FIG. S7. One dimensional lattice model with two sites and one link. The red arrows denote the flux boundary conditions at both ends of the lattice. The boundary conditions fix the allowed physical states by means of the Gauss law constraint.

A total of 5 qubits are needed to represent the total Hilbert space of this lattice system with spin value $S = 0.5$, namely two qubits per site and one qubit for the link in between, thus spanning a Hilbert space \mathcal{H} of dimension $2^5 = 32$. Furthermore, the background electric field $\theta = 0.5$ shifts the two allowed flux eigenvalues by $m_s \in \{-0.5, 0.5\} \rightarrow m_s \in \{0, 1\}$.

Note that out of these 32 states, only 5 states corresponds to physical states. The possible gauge invariant state configurations that are allowed by the the Gauss law constraint with this choice of boundary conditions are shown in Fig. S8 and in Fig. S9.

From these configurations it is clearly visible that our choice of the small spin value $S = 0.5$ with $\theta = 0.5$ does not affect the groundstate configurations of the model (S15): First, all gauge invariant states contain only fluxes in positive direction which is consistent with having possible flux values $m_s \in \{0, 1\}$. Second, the only physical state that is not representable with this choice of flux eigenvalues is the one with a particle-antiparticle pair connected by two flux strings. Nevertheless, such a state will always correspond to a higher energy state configuration than the two states in Fig. S8 and therefore, will not occur as a groundstate of this model. As a conclusion, choosing the values $S = 0.5$, $\theta = 0.5$ instead of $S = 1$, $\theta = 0$ allowed us to effectively remove one qubit in order to represent the gauge fields on the link.



FIG. S8. The groundstate configurations depending on the mass parameter m . When $m \gg g$ is big, then the flux string contains not enough energy in order to break (left). In the opposite case when $m \ll g$ is small, it is energetically more favourable to break the string by creating a particle-antiparticle pair (right).

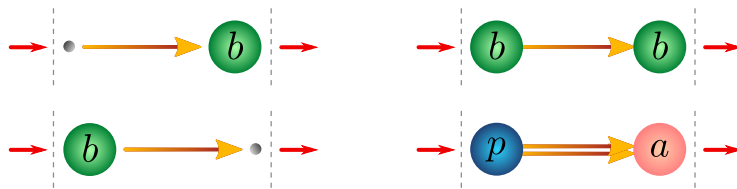


FIG. S9. Complete set of gauge invariant state configurations in addition to the two groundstates shown in Fig. S8. The state with a particle-antiparticle pair is not contained in the truncated state description for $S = 0.5$ with $\theta = 0.5$.

Now let us analyse the groundstate for varying mass parameter m . First, it is clear that the only possible groundstates that are to be considered are those depicted in Fig. S8 since all other gauge invariant states shown in Fig. S9 will always have a higher energy independently of the mass value m . As a next step, assume that the Hamiltonian (S15) would not contain any hopping term. In that case, the Hamiltonian is already diagonal and the groundstate would

depend on whether the mass term \hat{H}_{mass} or the electric term \hat{H}_{elec} has a smaller energy. The corresponding critical mass m_c is simply calculated by equating the total energy of the two state configurations in Fig. S8,

$$2 \cdot \left(m_c + \frac{r}{a}\right) = \frac{g^2 a}{2} \quad \Rightarrow \quad m_c = \frac{g^2 a}{4} - \frac{r}{a}. \quad (\text{S17})$$

and thus, the groundstate energy E_0 as a function of mass m will have a discontinuity in its first derivative [S61], see Fig. S10.

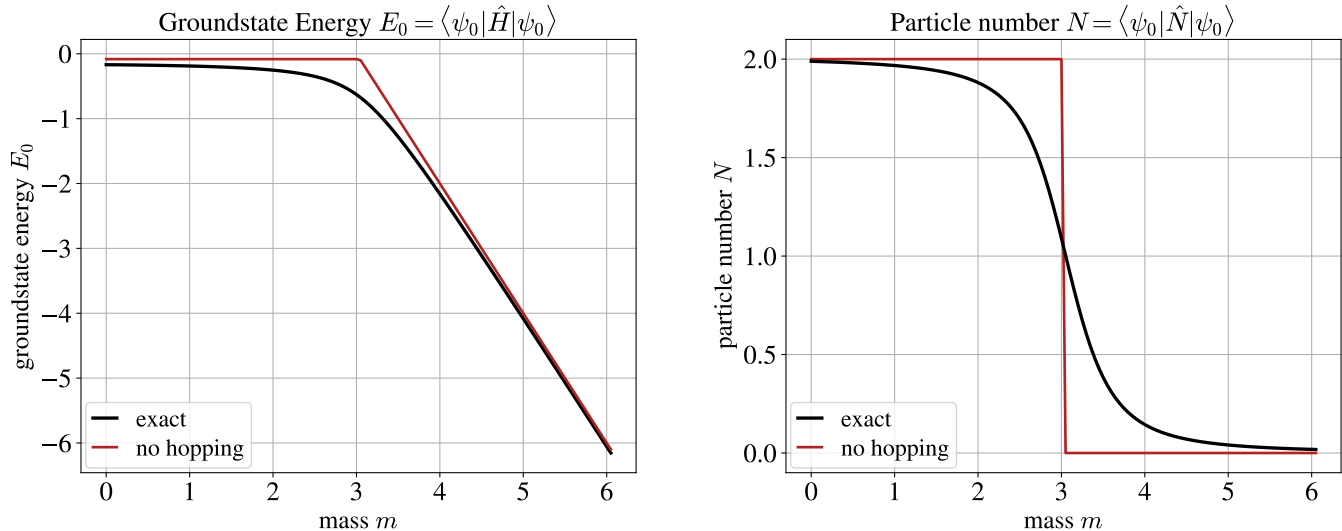


FIG. S10. The groundstate energy E_0 and the corresponding particle number N as a function of mass m . The chosen model parameters in (S15) are $g = 4$, $a = 1$, $r = 1$, $\lambda = 20$, $S = 0.5$, $\theta = 0.5$ resulting in a phase transition at the critical mass value $m_c = 3$. The black curves correspond to the full model (S15) while the red curves displays the groundstates for vanishing hopping term.

By adding the non-diagonal hopping term, the groundstate energy in the limiting regimes $m \gg m_c$ and $m \ll m_c$ stays approximately the same while in the critical mass regime $m \approx m_c$, strong quantum fluctuations are introduced that smooth out the groundstate energy and the particle number curves with $\hat{N} = \sum_n (\hat{\psi}_n \hat{\psi}_n + \mathbb{I})$ as is shown in Fig. S10. As a result, a phase transition is observed which corresponds to the flux string breaking.

Statistical sampling errors due to the gauge penalty term

A problem arises when evaluating the parametrized energy expectation value on a real quantum hardware since it can not be exactly calculated as in an ideal simulation, but the parametrized energy is rather statistically sampled from various measurements of the same circuit. This follows from the postulates of quantum mechanics where a measurement outcome of an observable randomly occurs with a probability determined by the wavefunction and thus, the outcome expectation value corresponds to an average of all the outcomes.

This fact can lead to problematic consequences in a VQE algorithm, especially due to the gauge penalty term \hat{H}_{gauge} with a large regularizing coefficient λ , since the statistical sampling errors might become too big leading to large non-zero energy contribution and thus, the correct groundstate energy can not be recovered anymore, although the gauge penalty term should in principle vanish for gauge invariant states.

In our lattice gauge theory models, the sampled expectation value $\langle \phi(\boldsymbol{\theta}) | \hat{H}_{\text{gauge}} | \phi(\boldsymbol{\theta}) \rangle$ of the gauge penalty term will in practice only approximately equal to zero for physical states. Since non-zero sampled expectation values will be proportional to the regularizing parameter λ which is usually chosen to be much larger than the other model parameters, the energy evaluations in a VQE algorithm will be largely disturbed.

To certify this hypothesis, we sampled the expectation value of the gauge penalty term $\lambda \hat{H}_{\text{gauge}}$ with $\lambda = 20$ with respect to an equal superposition of the two gauge invariant groundstates shown in Fig. S8 with increasing number of shots (i.e. measurements) by using IBM's `Qiskit QASM`-simulator [S57]. Each weighted Pauli string in the gauge penalty term was measured separately. The results are plotted in Fig. S11. It is observed that the statistical

fluctuations are of the same order of magnitude as the energy scale of the groundstate energies of the considered model (S15). Note that if one is interested in the groundstate only, the regularization value λ could in principle be chosen smaller (as long as it lifts the energy of the unphysical states to an amount which is bigger than the energy of the groundstate). However, higher excited states become important in a real-time evolution in general and thus, the regularization value must increase correspondingly to ensure that the dynamics remain physical [S60].

It is further shown in Fig. S12 how such statistical sampling errors increase for a one-dimensional lattice with increasing number of lattice sites. We observe an enhancement of the standard deviation with increasing system size, hinting that such statistical noise might become intractable for LGT models with large lattices.

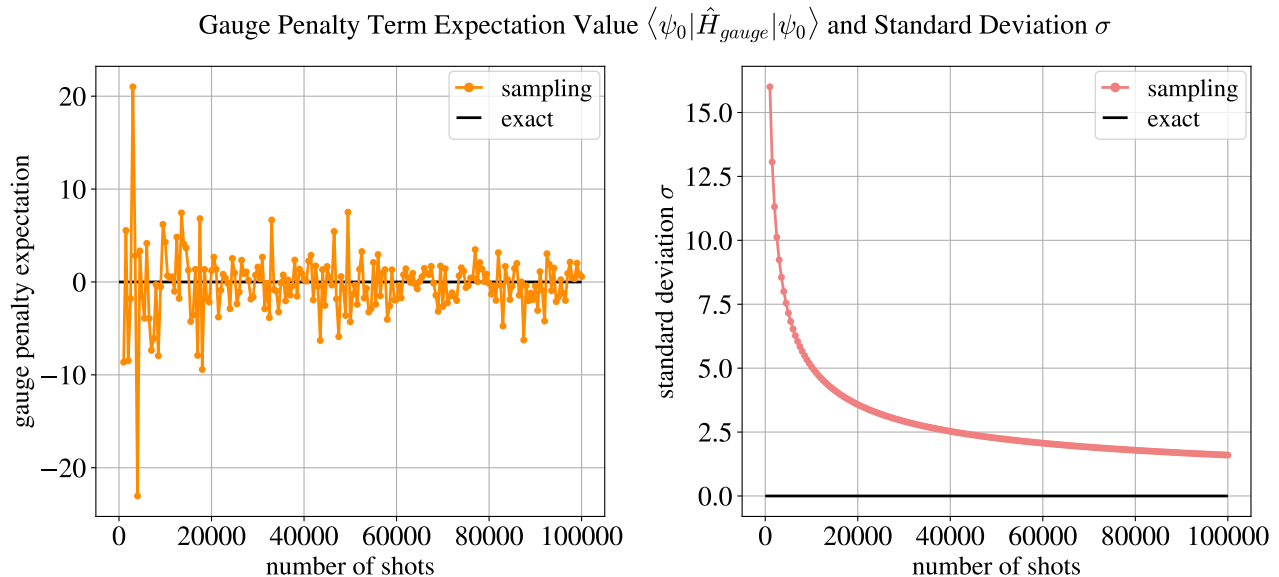


FIG. S11. Statistical sampling of the gauge penalty term expectation value (left) and the corresponding standard deviation (right) with respect to a superposition of gauge invariant states. The regularizing parameter $\lambda = 20$ gives rise to large statistical fluctuations around the theoretical zero expectation value.

The observed issue can be circumvented in different ways. First, it might happen that the weighted Pauli strings P which make up the gauge penalty term $\hat{H}_{gauge} = \sum_P \lambda_P P$ all commute with each other as is the case in a Jordan-Wigner fermion-to-qubit encoding of this term, for example. Then, the Pauli strings can all be simultaneously measured and therefore, the same state measurement outcome statistics can be used to evaluate the expectation value of all the Pauli strings in a *grouped* manner [S50, S51, S59], resulting in a vanishing statistical error. However, the exact form of the Pauli strings will depend on the specific encoding of the gauge and matter fields and the Pauli strings may not pairwise commute in general. Furthermore, the exact choice of grouping the Pauli string bases might affect the overall sampling efficiency of evaluation of the total Hamiltonian.

In our simulations we pursue a different strategy. Since we are working with a variational form that is gauge invariant by construction, there is in principle no need to additionally impose the Gauss law constraint as a penalty term at all, provided that the initial state $|\phi_{init}\rangle$ used in the VQE algorithm corresponds to a physical gauge invariant state configuration. As a result, the variational form samples only from the physical Hilbert space leading to the correct low-lying energy spectrum and thus, we will simply set the gauge penalty term to zero. It is observed that with vanishing gauge regularizing parameter $\lambda = 0$, the statistical fluctuations remain small compared to the energy scale set by the chosen model parameters.

Nevertheless, in practice there might be a small probability that the gauge invariant variational form *does* sample from a set of unphysical states depending on the form of the coupling matrices $A(\theta)$, $\Lambda(\theta)$ in (S13) due to Trotter approximation errors [S62]. The Trotter error in the approximation can be made arbitrarily small by increasing the number of Trotter steps at the cost of enlarging the circuit gate complexity.

There exists a third approach as was already pointed out in [S60] that makes use of so-called Gauss law oracles [S34]. Such Gauss law oracles can be included in the VQE algorithm as a subroutine to check whether the produced variational form $|\phi(\theta)\rangle$ is actually gauge invariant or not. In that way, one can make sure that the small error produced by the Trotterization does not lead to an unphysical energy spectrum even when the gauge penalty term is set to zero.

Normalized Standard Deviation σ/λ of the Gauge Penalty Term $\langle \psi_0 | \hat{H}_{gauge} | \psi_0 \rangle$

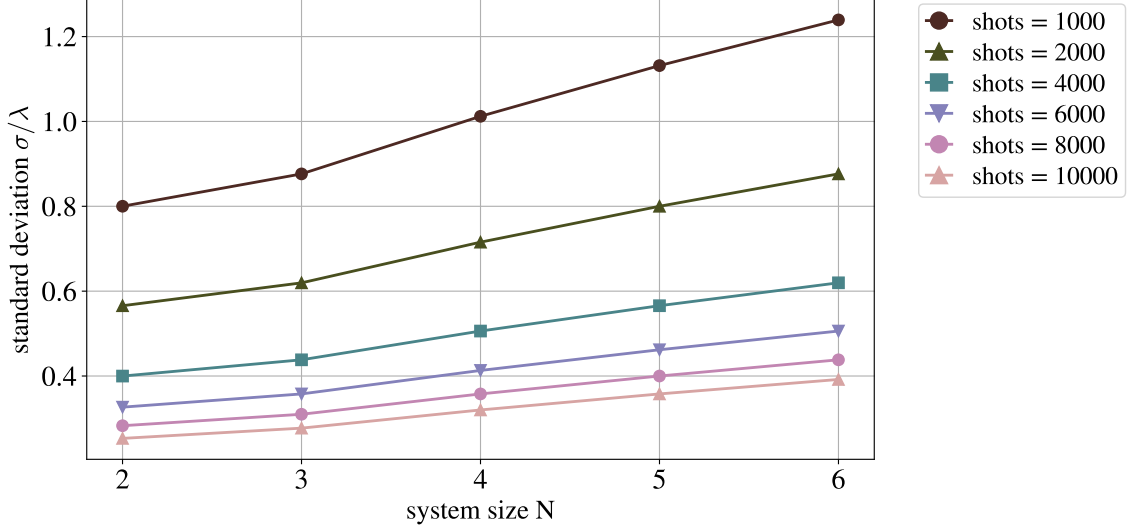


FIG. S12. Standard deviation of the statistical sampling error in measuring the gauge penalty term expectation value in $d = 1$ for growing system size (i.e., number of lattice sites) N for different fixed number of shots. The regularization parameter is chosen as $\lambda = 20$.

Quantum hardware simulation

As already mentioned above (or as can be directly observed in the circuit (S19)), the first and the last fermionic qubits "fermionic₀" and "fermionic₃" are not entangled with the other qubits since only single-qubit gates are applied to these two qubits. As a consequence, the parametrized wavefunction $|\psi(\theta)\rangle$ has a product form with respect to these two qubits which allows us to factorize the parametrized energy as

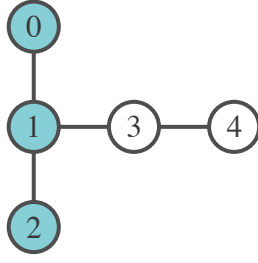
$$\begin{aligned}
 E(\theta) &= \langle \phi(\theta) | \hat{H} | \phi(\theta) \rangle = \sum_{P \in \mathcal{P}_5} \lambda_P \langle \phi(\theta) | P | \phi(\theta) \rangle \\
 &= \sum_{P \in \mathcal{P}_5} \lambda_P \langle \phi_0(\theta) | P_0 | \phi_0(\theta) \rangle \cdot \langle \phi_3(\theta) | P_3 | \phi_3(\theta) \rangle \cdot \langle \phi_{124}(\theta) | P_{124} | \phi_{124}(\theta) \rangle \\
 &\text{with } P = P_0 \otimes P_1 \otimes P_2 \otimes P_3 \otimes P_4, \quad |\phi(\theta)\rangle = |\phi_0(\theta)\rangle \otimes |\phi_3(\theta)\rangle \otimes |\phi_{124}(\theta)\rangle \\
 &\text{and } \hat{H} = \sum_{P \in \mathcal{P}_5} \lambda_P P, \quad \lambda_P \in \mathbb{R}
 \end{aligned} \tag{S18}$$

for Pauli strings $P \in \mathcal{P}_5$ that act on a 5-qubit register with $P_{124} \equiv P_1 \otimes P_2 \otimes P_4$ and where $|\phi_{124}(\theta)\rangle$ denotes the wavefunction corresponding to the qubits with index 1, 2 and 4. The single-qubit terms of the form $\langle \phi_i(\theta) | P_i | \phi_i(\theta) \rangle$ can be efficiently calculated on a classical computer since they basically correspond to 2×2 matrix multiplications. As a conclusion, only the non-trivial entangled part of the wavefunction $|\phi_{124}(\theta)\rangle$ will have to be evaluated on the quantum device.

This observation will be exploited in our quantum simulation in order to reduce the required qubit resources from 5 to 3 qubits, thereby effectively lowering noise errors that are present in a simulation with real quantum hardware.

With the preliminary work in the previous paragraphs, we consequently ran a separate VQE algorithm in order to search the groundstate of the model for each distinct mass value m by using the specific variational form (S13) with three parameters, and whose implementing circuit takes the form (S19). The initial state $|\phi_{\text{init}}\rangle$ was chosen as the gauge invariant bare vacuum state with no particles on the sites and one unit of positive flux on the link.

The complete quantum circuit was run on the *ibmq_vigo* superconducting machine which is characterized in Fig. S13. At each iteration step of the VQE algorithm, the parametrized circuit was repeated 8000 times (8000 shots) in order to achieve a small sampling error for the energy and particle number expectation value. For the classical optimization routine, the *SPSA* optimization algorithm (100 optimization steps, without calibration) was used which has been proposed for minimizing noisy energy functions [S51]. Furthermore, we applied a measurement error mitigation



Qubit	Single-Qubit U_2 error rate	Readout error
q_0	$3.928 \cdot 10^{-4}$	$1.20 \cdot 10^{-2}$
q_1	$4.103 \cdot 10^{-4}$	$1.00 \cdot 10^{-2}$
q_2	$4.581 \cdot 10^{-4}$	$1.30 \cdot 10^{-2}$
Connectivity	$CNOT$ error rate	
$q_0 \longleftrightarrow q_1$	$7.841 \cdot 10^{-3}$	
$q_1 \longleftrightarrow q_2$	$8.126 \cdot 10^{-3}$	

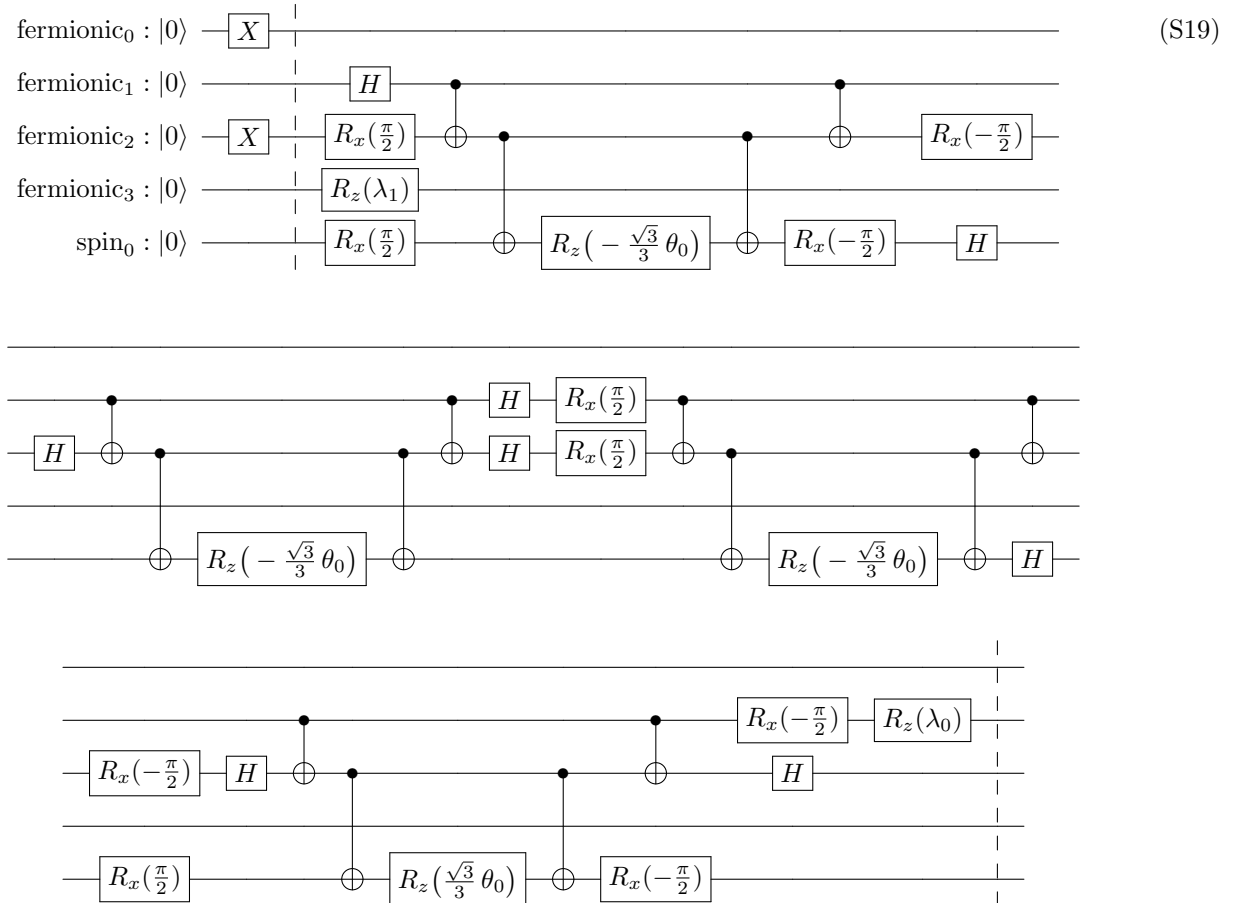
FIG. S13. The *ibmq_vigo* quantum hardware with the qubit configuration topology (left) and the corresponding gate- and readout error rate specifications (right). The three qubits coloured in blue correspond to the qubits used in the quantum simulation.

scheme that is included in IBM's Qiskit software development framework in order to reduce noise errors due to the measurement readout process [S57].

GAUGE INVARIANT VARIATIONAL FORM: CIRCUIT EXAMPLE

Here, we display the explicit quantum circuit representing the variational form (S13) with 3 variational parameters ($\lambda_0, \lambda_1, \theta_0$) that was used in the VQE simulations for the lattice QED model (S15) on a $d = 1$ dimensional lattice with $M = 2$ sites and with a spin value $S = 1/2$ in the quantum link model truncation of the gauge electric fields.

The first two X gates before the first barrier generate the gauge-invariant bare vacuum state with zero particles on the sites and positive flux on the link in between. The following variational form visibly consists of four Pauli strings $I_0 X_1 Y_2 I_3 Y_4$, $I_0 X_1 X_2 I_3 X_4$, $I_0 Y_1 Y_2 I_3 X_4$, and $I_0 Y_1 X_2 I_3 Y_4$ which all commute with each other, thus implying a vanishing Trotter approximation error.



GRAPHICAL NOTATION FOR LATTICE QED

Here, we shortly introduce a graphical notation used to describe quantum state configurations in the Dirac spinor representation on a lattice. The graphical notation allows us to depict the different quantum states of the total Hilbert space \mathcal{H}_{YM} in the basis that we are working with.

In the following, we choose a basis for the fermionic matter fields such that the mass operator $\hat{M}_x = m \hat{\psi}_x \hat{\psi}_x$ and the charge operator $\hat{Q}_x = \hat{\psi}_x^\dagger \hat{\psi}_x$ are diagonal on each lattice site x . On a single site, there exist four possible states: a vacuum state with no particles corresponding to an empty site, a particle state, an antiparticle state and a state containing both particle and antiparticle which fully occupy the lattice site. These states and the corresponding particle number and charge eigenvalues are listed in Fig. S14.

•	empty site	$N = \langle \hat{\psi} \hat{\psi} + 1 \rangle = 0$	$Q = \langle \hat{\psi}^\dagger \hat{\psi} - 1 \rangle = 0$
	particle	$N = \langle \hat{\psi} \hat{\psi} + 1 \rangle = 1$	$Q = \langle \hat{\psi}^\dagger \hat{\psi} - 1 \rangle = +1$
	antiparticle	$N = \langle \hat{\psi} \hat{\psi} + 1 \rangle = 1$	$Q = \langle \hat{\psi}^\dagger \hat{\psi} - 1 \rangle = -1$
	fully occupied site	$N = \langle \hat{\psi} \hat{\psi} + 1 \rangle = 2$	$Q = \langle \hat{\psi}^\dagger \hat{\psi} - 1 \rangle = 0$
—	empty link	$\langle \hat{L} \rangle = 0$	
	positive flux	$\langle \hat{L} \rangle = +1$	or $+\frac{1}{2}$
	negative flux	$\langle \hat{L} \rangle = -1$	or $-\frac{1}{2}$

FIG. S14. Graphical notation toolkit for depicting the quantum states on single lattice sites and links. The four fermionic states on a site are characterized by a particle number N and a charge Q eigenvalue, while the link states correspond to a fixed flux eigenvalue L . The link states corresponding to a flux value $L > 1$ ($L < -1$) are depicted by stacking L right (left) pointing arrows on top of each other. For integer spin S , stacking a right and a left pointing arrow results in the empty link state. For half-integer spin S , the link flux values must be half-integers as well and empty link states with flux value $L = 0$ are not allowed. A general quantum state on the lattice is obtained by combining the single pieces.

For the gauge fields that reside on the links, we select a basis of the quantum states which corresponds to the eigenbasis of the electric flux operator $\hat{L}_{(x,k)}$ for every link (x,k) . The gauge fields are truncated using an embedding spin algebra in a quantum link model [S26]. On a single link, the corresponding Hilbert space is of dimension $2S + 1$ where S is a positive integer or half-integer $S = \frac{1}{2}, 1, \frac{3}{2}, 2, \dots$ and the possible flux eigenvalues m_s of $\hat{L}_{(x,k)}$ are restricted by the spin value S such that $m_s \in \{-S, -S + 1, \dots, S - 1, S\}$. Note that for a fixed (half-)integer spin values S , the possible flux value m_s are (half-)integers as well. The graphical symbols describing these states are shown in Fig. S14.

A general quantum state in the total Hilbert space \mathcal{H} corresponds to a specific combination of the different states on all the lattice sites and links. However, only a small fraction of these combinations are physically allowed by the local Gauss law constraints

$$\hat{G}_x |\phi_{\text{phys}}\rangle = 0 \quad \hat{G}_x = \sum_k \left(\hat{L}_{(x,k)} - \hat{L}_{(x-k,k)} \right) - \psi_x^\dagger \psi_x \quad \forall x .$$

In Fig. S15, we list a basic set of quantum state configurations for integer spin values S which fulfill the Gauss law constraint \hat{G}_x on a single lattice site x and are thus gauge invariant. Any physical state $|\phi_{\text{phys}}\rangle \in \mathcal{H}^{\text{phys}} \subset \mathcal{H}$ is then necessarily given by a combination of these gauge invariant state configurations.

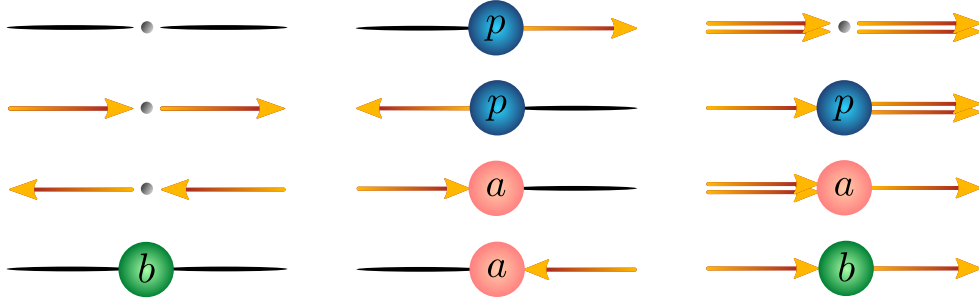


FIG. S15. A subset of gauge invariant state configurations for integer spin values S . The Gauss law constraint implies the following rules: An empty site "•" and a fully occupied site "b" behave in the same manner since both states have a zero net total charge Q and therefore do not change the flux values on the links. A particle state " p " emits one flux unit in an arbitrary direction while an antiparticle state " a " absorbs one unit of flux from an arbitrary direction. A physical state on the lattice corresponds to a combination of these configurations.



FIG. S16. A gauge invariant state configuration for $S = \frac{1}{2}$. A particle " p " of charge $Q = 1$ emits two arrows of flux $\pm \frac{1}{2}$ while an antiparticle " a " of charge $Q = -1$ absorbs two such arrows.